

Microstructural enrichment functions based on stochastic Wang tilings

Jan Novák^{a,b,*}, Anna Kučerová^c, Jan Zeman^c

^a*School of Civil and Environmental Engineering, University of New South Wales, NSW 2052, Sydney, Australia*

^b*Centre for Integrated design of Advanced Structures, Faculty of Civil Engineering, Czech Technical University in Prague, Thákurova 7, 166 29 Praha 6, Czech Republic*

^c*Department of Mechanics, Faculty of Civil Engineering, Czech Technical University in Prague, Thákurova 7, 166 29 Praha 6, Czech Republic*

Abstract

This paper presents a new approach to determining microstructural enrichment functions to local fields in non-periodic heterogeneous materials with applications in Partition of Unity and Hybrid Finite Element schemes. It is based on a concept of aperiodic tiling by the Wang tiles, designed to produce microstructures morphologically similar to original media and enrichment functions that satisfy the underlying governing equations. An appealing feature of this approach is that the enrichment functions are defined only on a small set of square tiles and extended to larger domains by an inexpensive stochastic tiling algorithm, thereby circumventing the need for simulations of large heterogeneous bodies. Feasibility of the proposed methodology is demonstrated on local constructions of the stress fields in two-dimensional particulate media.

Keywords: Tiling; Microstructure optimization; Enrichment functions; Partition of Unity; Trefftz method; FFT-based solvers

1. Introduction

A detailed mechanical analysis of materials with complex microstructure that accounts for the full resolution of microstructural heterogeneities by using classical

*Corresponding author. Tel.: +61-293-855-022

Email addresses: jan.novak@unsw.edu.au, novakj@cml.fsv.cvut.cz (Jan Novák), anicka@cml.fsv.cvut.cz (Anna Kučerová), zemanj@cml.fsv.cvut.cz (Jan Zeman)

numerical approaches as the Finite Element method has been found computationally prohibitive [1]. To overcome this, one option consists of modeling a macroscopic problem with the help of homogenization techniques based on effective material properties [2, 3, 4]. However, this may lead to a considerable loss of information about the fine scale behavior, thereby resulting in an inaccurate assessment of microstructural effects on macroscopic response.

An alternative strategy free of this phenomenon, yet computationally tractable, proceeds from enrichment based techniques, such as Partition of Unity (PU) [5] and Hybrid Finite Element (HFE) methods [6]. In these environments the approximation properties of standard finite element spaces is enhanced by introducing a-priori knowledge of subscale behaviour into the system through a class of enrichment functions [7, 8, 9, 10, 11, 12, 13]. These are, however, associated with additional degrees of freedom and nested computational demands to solve a particular subscale boundary value problem.

The objective of this work is thus to develop a new algorithm that allows for extending the local constructions from computationally tractable samples to entire macroscopic domains. The algorithm keeps generated enrichment fields continuous across subscale sample boundaries and consistent in terms of statistical properties of original and reconstructed material morphologies. It is based on a small number of Wang tiles [14, 15, 16] and the stochastic tiling concept introduced by Cohen et al. [17].

In 1961, Hao Wang introduced a tiling concept involving square tiles of different codes on their edges referred to as Wang tiles [14]. The tiles are connected together so that the adjacent edges have the same code and permit computationally efficient graphic reproduction of morphological patterns in real time [17, 16, 18, 15]. Their desirable aesthetic properties are attributed to the aperiodicity of the tilings, whereas the low computational effort results from the use of a small number of tiles to compress the entire morphological information [19].

Here, we exploit and extend these principles to provide a basis for an efficient generation of microstructure-based enrichment functions applicable in PU- or HFE-based algorithms for heterogeneous media. In order to meet additional criteria arising from such constructions, the Simulated annealing-based optimization [20, 21] is used to arrive at optimal tile sets. The performance of the method is illustrated on the construction of tile-based stress fields in a particulate two phase composite medium with linear elastic phases.

The paper structure is as follows. The concept of stochastic Wang tiling is described in Section 2. A discussion on the optimization procedure based on prescribed statistical descriptors and compatibility of mechanical fields on contiguous tile edges

is given in Section 3. Section 4 comprises numerical examples demonstrating the performance of the proposed approach. This is complemented with discussion of the two strategies to incorporate the enrichment functions into finite element schemes in 5. Final remarks on the current developments and future plans are assembled in Section 6. Finally, in Appendix A, we present a brief overview of the stress analysis algorithm.

The following nomenclature is used in the text. Scalar quantities are denoted by plain letters, e.g. a or A , matrices by bold serif font, e.g. \mathbf{a} or \mathbf{A} , and tensorial quantities by bold letters, e.g. \mathbf{a} or \mathbf{A} . In addition, we adopt the Mandel representation of symmetric second- and fourth-order tensors \mathbf{a} and \mathbf{A} , e.g. [22], so that

$$\mathbf{a} = \begin{bmatrix} a_{11} \\ a_{22} \\ \sqrt{2}a_{12} \end{bmatrix}, \quad \mathbf{A} = \begin{bmatrix} A_{1111} & A_{1122} & \sqrt{2}A_{1112} \\ A_{2211} & A_{2222} & \sqrt{2}A_{2212} \\ \sqrt{2}A_{1211} & \sqrt{2}A_{1222} & A_{1212} \end{bmatrix}$$

in the two-dimensional setting.

2. Aperiodic tilings by sets of Wang tiles

Consider the two dimensional Euclidean space \mathbb{R}^2 discretized by a regular square grid. Each grid cell contains specific morphological patterns that are compatible on contiguous boundaries (Fig. 1(b)). If there are no missing cells inside the domain, the discretization is called valid tiling and a single cell is referred to as the Wang tile (Fig. 1(a)) [14]. The tiles have different codes on their edges, enumerated here by small Greek letters, and are not allowed to rotate during the tiling procedure. The number of distinct tiles is limited, though arranged in such a fashion that no sub-sequence periodically repeats. The set of all distinct tiles is referred to as the tile set. Sets that enable uncountably many, always aperiodic, tilings are called aperiodic sets [16]. The assumption of strictly aperiodic sets can be relaxed, though still being capable to tile the plane aperiodically, e.g., when utilizing the algorithm due to Cohen et al. [17] briefly described in the following section. Note that such tilings are substantial generalizations of periodic paving algorithms, which use identical tiles formed by unit cells.

2.1. Tile set setup

Favorable properties of a tile set to control nested repetitive effects proceed from the tile and edge code diversity (Fig. 1(a)). The number of edge codes n_i^c in the i -th

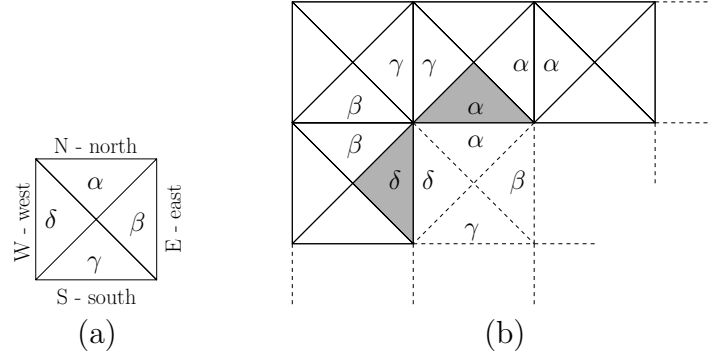


Figure 1: (a) A Wang tile with edge codes $\{\alpha, \beta, \gamma, \delta\}$, (b) an example of aperiodic valid tiling with highlighted connectivity across south-eastern and north-western edges.

spatial direction of the Cartesian coordinates may be chosen arbitrarily, while the number of tiles n^t must satisfy

$$n^t = n^{\text{NW}} \sqrt{n^{\text{cs}}}, \quad (1)$$

where $n^{\text{cs}} = (n_1^c n_2^c)^2$ is the number of tiles in the complete set and $n^{\text{NW}} = 2, \dots, \sqrt{n^{\text{cs}}}$ stands for the number of admissible pairs of north-western (NW) edge codes.

When designing a tile set, one chooses a particular number of edge codes n_1^c and n_2^c . The complete set of n^{cs} tiles is created by mutually permuting the codes. In order to tile the plane, the south-eastern edge codes must match those assigned to NW edges, Fig. 1(b). Thus, the created tiles are sorted according to NW combinations. Finally, a desired number of tiles is chosen using Eq. (1), in such a way that n^{NW} of tiles is taken from each NW group. The emerging set of tiles is referred to as $Wn^t/n_1^c - n_2^c$ in the sequel; moreover, we denote the relative frequency of occurrence of the c -th code in the tile set by q_c , see Fig. 2.

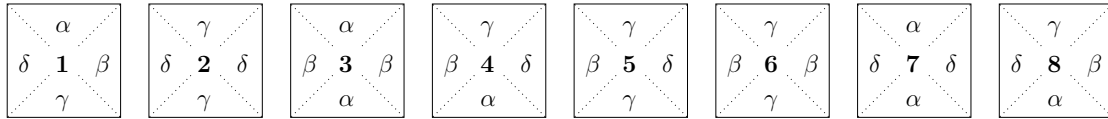


Figure 2: Tile set W8/2-2 consisting of 8 tiles with 2 vertical $\{\alpha, \gamma\}$ and 2 horizontal $\{\beta, \delta\}$ edge codes with equal frequencies of occurrence $q_\alpha = q_\beta = q_\gamma = q_\delta = \frac{1}{4}$ [17].

2.2. Stochastic tiling algorithm

Since there are n^{NW} tiles associated to each NW group, index of the new tile to be placed is selected randomly from the set $\{1, \dots, n^{\text{NW}}\}$ with the uniform probability.

Beforehand, one must select an appropriate NW group compatible with the eastern code of a previously placed tile and the southern code of the tile just above the one to be placed (outer edges α and δ of shaded areas in Fig. 1(b)). Aperiodicity of the resulting tiling is guaranteed when assuming that the random generator never returns a periodic sequence of numbers and that each NW group contains at least two distinct tiles [17].

3. Designing optimal tiles

To simplify the exposition, we limit our attention to two-phase composite media formed by a matrix phase and equi-sized disks of radius ρ and the microstructure representation built on the Wang tile set W8/2-2.¹ The location of the disks within the tiles has to be optimized to achieve (i) good approximation of the original microstructure in terms of a given morphological descriptor (Section 3.1) and (ii) microstructures that guarantee the compatibility of mechanical fields on contiguous tile edges,² see Section 3.2. Such criteria originate from different perspectives. The first goal aims at capturing the dominant spatial features of original media and as such it is closely related to microstructure reconstruction or compression algorithms developed, e.g. in [23, 24, 25, 26, 27, 28, 29]. The latter criterion ensures that the tiling-generated fields comply with the governing differential equations and can be used as basis functions in the aforementioned numerical schemes, see Section 5.

3.1. Statistical properties of the microstructure

The most common class of statistical descriptors embodies a set of n -point probability functions, applicable to generic heterogeneous media [30]. In this paper, the focus is on the two-point probability functions, which capture primary phenomena as the phase volume fractions, characteristic microstructural length(s), long-range order information and (an)isotropy.

Consider a domain $\mathcal{D} \subset \mathbb{R}^2$ occupied by a two-phase heterogeneous material discretized by a regular lattice with $N_1^{\mathcal{D}} \times N_2^{\mathcal{D}}$ pixels, indexed by $\mathbf{k} \in \mathcal{K}$ with

$$\mathcal{K} = \left\{ \mathbf{m} \in \mathbb{Z}^2 : -\frac{N_i^{\mathcal{D}}}{2} < m_i \leq \frac{N_i^{\mathcal{D}}}{2}, i = 1, 2 \right\}. \quad (2)$$

¹The set W8/2-2 has been chosen since it is the simplest one that allows for aperiodic patterns in the stochastic sense [17]. Note that most of the steps of the tile set design can be directly generalized to arbitrary media and more complex tile sets.

²Henceforth, the term “tiling” stands for “valid tiling” exclusively, thereby excluding invalid tilings from the consideration.

The distribution of individual phases (disks and matrix) within \mathcal{D} is quantified by the characteristic function $\chi(\mathbf{k})$, which equals 1 when \mathbf{k} is occupied by the disk phase and is 0 otherwise, cf. Fig. 3(a). Assuming a periodic³ ergodic medium, the two-point probability function $S_2 : \mathcal{K} \rightarrow [0, 1]$ is then defined as [30]

$$S_2(\mathbf{k}) = \frac{1}{N^{\mathcal{D}}} \sum_{\mathbf{m} \in \mathcal{K}} \chi(\mathbf{m}) \chi([\mathbf{k} + \mathbf{m}]_{\mathcal{K}}), \quad (3)$$

where $N^{\mathcal{D}} = N_1^{\mathcal{D}} N_2^{\mathcal{D}}$ and $[\bullet]_{\mathcal{K}}$ denotes the \mathcal{K} -periodic extension. Noticing that (3) has the structure of circular correlation, the two-point probability function can be efficiently evaluated using Fast Fourier Transform techniques, see e.g. [31].

According to its definition, $S_2(\mathbf{k})$ quantifies the probability that two arbitrary points separated by \mathbf{k} will both be located at the disk phase when randomly selected from \mathcal{K} . Denoting by ϕ the disk volume fraction, $0 \leq \phi \leq 1$, the two-point probability function satisfies $S_2(\mathbf{0}) = \phi$. Moreover, $S_2(\mathbf{k}) \simeq \phi^2$ for $\|\mathbf{k}\| \gg \rho$ indicates that the medium does not exhibit artificial long-range order effects, cf. Fig. 3(b).

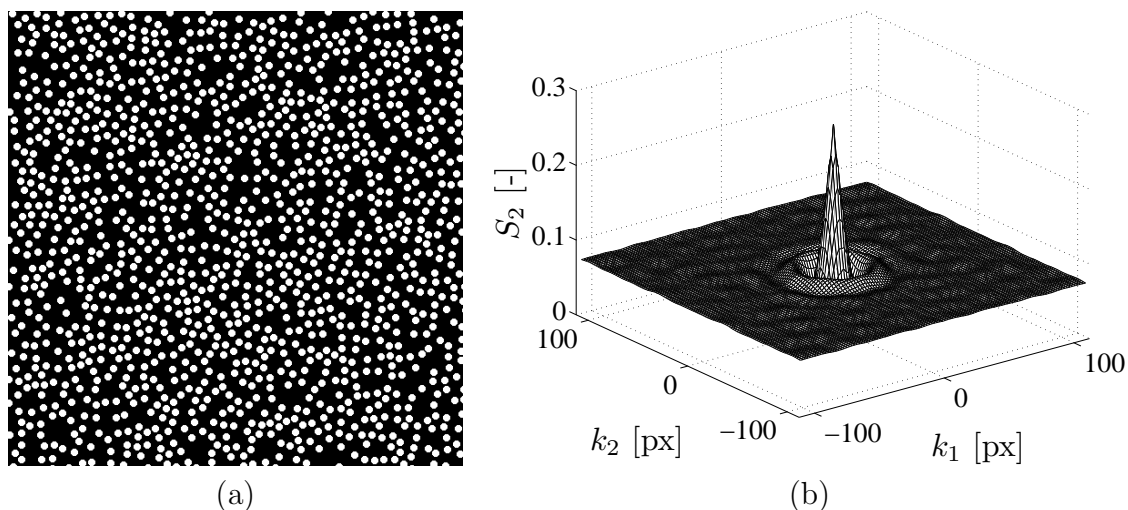


Figure 3: (a) An example of two-phase medium formed by equilibrium distribution of 1,300 equi-sized disks of volume fraction 26.8% and (b) the two-point probability function S_2 ; the sample is discretized with $1,000 \times 1,000$ pixels and each disk has the radius of 8 pixels.

The following procedure is adopted to determine the two-point probability function for the tile-based microstructure. First, the set W8/2-2 is used to assemble a

³Note that periodicity is considered here for the sake of computational efficiency. The tiling-generated microstructure is always aperiodic.

small tiling $\mathcal{D}_S \subset \mathbb{R}^2$ consisting of 4×4 tiles, Fig. 4(a). Here, each tile appears with the same frequency in order to suppress artificial fluctuations in volume fractions. The domain \mathcal{D}_S is discretized by an $N_1^{\mathcal{D}_S} \times N_2^{\mathcal{D}_S}$ regular grid with the same lattice spacing as in the original microstructure, so that $N_i^{\mathcal{D}_S} < N_i^{\mathcal{D}}$.

Given a parameter matrix $\mathbf{p} \in \mathcal{P}$ quantifying positions of individual disks, as discussed later on, the tile-based morphology is quantified by the two-point probability function $\tilde{S}_2 : \mathcal{P} \times \mathcal{K} \rightarrow [0, 1]$, and its proximity to the target microstructure is given by

$$f_S(\mathbf{p}) = \frac{1}{N^{\mathcal{D}_S}} \sum_{\mathbf{k} \in \mathcal{K}^{\mathcal{D}_S}} \left(S_2(\mathbf{k}) - \tilde{S}_2(\mathbf{p}, \mathbf{k}) \right)^2, \quad (4)$$

where $N^{\mathcal{D}_S}$ and $\mathcal{K}^{\mathcal{D}_S}$ are defined analogously as for the original medium \mathcal{D} .

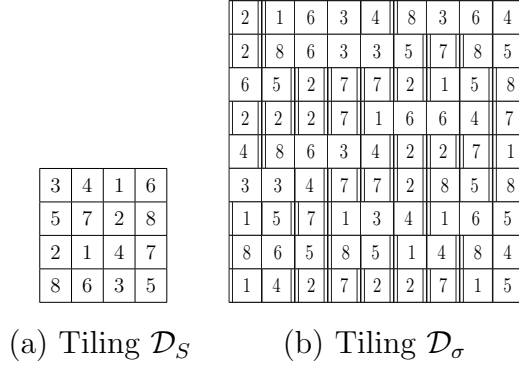


Figure 4: Valid tilings used in optimization with respect to (a) two-point probability functions and (b) stress fields; highlighted vertical edges in (b) correspond to edge set Σ^δ containing 50 equivalent edges of code δ .

3.2. Compatibility of mechanical fields

The second, yet more complex, goal is to find the tile set morphology that ensures the compatibility of physical fields obtained by the tiling algorithm. In particular, we choose the stress $\boldsymbol{\sigma}$ as the quantity of interest, since it is typically used to predict the onset of inelastic behavior. Again, for the computational convenience, the optimization is performed for a relatively small representative tiling \mathcal{D}_σ , Fig. 4(b), discretized into a $N_1^{\mathcal{D}_\sigma} \times N_2^{\mathcal{D}_\sigma}$ points, periodic on external boundaries.

Assigning the elastic properties to the matrix and the disks, the stress analysis proceeds as follows. First, the distribution of individual phases within the tile set \mathcal{D}_σ is determined for a parameter vector \mathbf{p} . Next, using the algorithm outlined in

Appendix A, the tiling is subjected to an average strain field

$$\mathbf{E} = \begin{bmatrix} E_{11} & E_{22} & \sqrt{2}E_{12} \end{bmatrix}^\top \quad (5)$$

that results in the distribution of local stress fields

$$\boldsymbol{\sigma}^{(i)}(\mathbf{p}, \mathbf{k}) = \begin{bmatrix} \sigma_{11}^{(i)}(\mathbf{p}, \mathbf{k}) & \sigma_{22}^{(i)}(\mathbf{p}, \mathbf{k}) & \sqrt{2}\sigma_{12}^{(i)}(\mathbf{p}, \mathbf{k}) \end{bmatrix}^\top, \quad \mathbf{k} \in \mathcal{K}^{\mathcal{D}_\sigma}. \quad (6)$$

Here, $\mathcal{K}^{\mathcal{D}_\sigma}$ is defined analogously to (2), and the superscript $\bullet^{(i)}$ denotes the stress determined for the i -th loadcase, $i = 1, 2, 3$, obtained by successively setting each component of the average strain field \mathbf{E} to 1, while the remaining components equal to 0.

Similarly to the original Wang idea, the compatibility of the resulting stress fields will be enforced via edges. In particular, for each edge code $c = 1, 2, \dots, n^c$ with $n^c = n_1^c + n_2^c$, we identify a set Σ_c , formed by contiguous edges $\Sigma_{c,j}, j = 1, \dots, n_c^\Sigma$ of identical code c and length ℓ , see Fig. 4(b).⁴ The stress incompatibility for the i -th loadcase and edge code c is quantified by

$$\llbracket \sigma_c^{(i)} \rrbracket(\mathbf{p}) = \frac{1}{\ell} \sum_{s=1}^{\ell} \left\| \max \left\{ \mathbf{T}_c^{(i)}(\mathbf{p}, \boldsymbol{\Sigma}_{c,j}(s)) \right\}_{j=1}^{n_c^\Sigma} - \min \left\{ \mathbf{T}_c^{(i)}(\mathbf{p}, \boldsymbol{\Sigma}_{c,j}(s)) \right\}_{j=1}^{n_c^\Sigma} \right\|_1, \quad (7)$$

where $\mathbf{T}_c^{(i)} \in \mathbb{R}^2$ denotes the traction vector acting at Σ_c determined from $\boldsymbol{\sigma}^{(i)}$, $\boldsymbol{\Sigma}_{c,j}(s) \in \mathcal{K}^{\mathcal{D}_\sigma}$ gives the coordinate of the s -th pixel at the j -th edge with code c , max and min operations are understood component-wise and $\|\mathbf{x}\|_1 = \sum_i |x_i|$. Collecting the contributions from all loadcases and codes, the objective function becomes

$$f_\sigma(\mathbf{p}) = \sum_{i=1}^3 \sum_{c=1}^{n^c} \llbracket \sigma_c^{(i)} \rrbracket(\mathbf{p}). \quad (8)$$

3.3. Microstructure parametrization

In general, the microstructure representation is based on a given Wang tile set consisting of n^t tiles of the edge length $\ell \in \mathbb{N}$, in which we distribute n^d disks of radius

⁴Notice that \mathcal{D}_σ must contain all admissible combinations of tile pairs from the set $Wn^t/n_1^c - n_2^c$ sharing all edge codes. For example, for the W8/2-2 tile set, Fig. 2, there are 16 combinations of basic tiles sharing the code $\delta : \{2-1, 2-2, 2-7, 2-8, 4-1, 4-2, 4-7, 4-8, 5-1, 5-2, 5-7, 5-8, 7-1, 7-2, 7-7, 7-8\}$ and therefore $n_\delta^\Sigma = 50 \geq 16$, cf. Fig. 4(b).

ρ . The d -th disk is represented by a triplet $\{t^{[d]}, x_1^{[d]}, x_2^{[d]}\}$, where $t^{[d]} \in \{1, \dots, n^t\}$ denotes the tile index and $x_j^{[d]} \in \{1, \dots, \ell\}$ specifies the position of the d -th disk within the tile at the j -th direction. The aforementioned parameter vector \mathbf{p} is obtained as a collection of these data:

$$\mathbf{p} = \left[t^{[d]}, x_1^{[d]}, x_2^{[d]} \right]_{d=1}^{n^d}. \quad (9)$$

This also implicitly defines the parameter space \mathcal{P} .

In an admissible configuration, the disks do not overlap each other or corners of tiles being associated with. The first constraint reflects the given feature of the original microstructure, Fig. 3(a), whereas the latter one arises as an artifact intrinsic to the edge-based tiling algorithm, e.g., [17]. In addition, to maintain the morphological compatibility, any disk intersecting the edge of a given code is also associated to tiles sharing the same code, cf. Fig. 5. To emphasize this, we encode a particular configuration as $n^d \{n_c^\Gamma\}_{c=1}^{n^c}$, where n_c^Γ denotes the number of disks intersecting the edge of code c .

3.4. Optimization procedure

In fact, the goals represented by objective functions (4) and (8) are conflicting. Minimizing only with respect to the two-point probability function results in non-compatible stress fields, whereas the latter criterion drives the system to a periodic distribution of disks on tile edges. To achieve a compromise solution, we introduce a combined objective function in the form

$$f(\mathbf{p}) = w f_S(\mathbf{p}) + f_\sigma(\mathbf{p}), \quad (10)$$

where w denotes a weighting factor to be estimated by a trial-and-error procedure. The minimization of the objective function (10) is performed by the well-established Simulated Annealing method [20, 21], extended by a re-annealing phase to escape from local extremes, e.g. [32].

Given the number of disks n^d and the target volume fraction ϕ , we initiate the algorithm by determining the number of edge disks n_c^Γ related to the c -th code and the tile edge length ℓ . However, this problem is not trivial due to the multiple presence of the code-related disks, recall Fig. 5. Thus, we are able to resolve it only via a heuristic procedure outlined next. We estimate the total area of disks within the tile set as

$$\tilde{A} \approx \left(n^d + \sum_{c=1}^{n^c} (2n^t q_c - 1) n_c^\Gamma \right) A^d, \quad (11)$$

with A^d denoting the area of a single disk (in square pixels). This corresponds to the tile-based volume fraction

$$\tilde{\phi} \approx \frac{\tilde{A}}{n^t \ell^2}, \quad (12)$$

which should be as close to the target value ϕ as possible. In addition, we impose the condition

$$\frac{n^d - \sum_{c=1}^{n^c} n_c^\Gamma}{(\ell - 2\rho)^2} \approx \frac{n^t \sum_{c=1}^{n^c} q_c n_c^\Gamma}{2\rho(\ell - \rho)}, \quad (13)$$

matching the local volume fractions of disks intersecting and non-intersecting edges of the tile set. Thus, given the number of disks attached to codes $\{n_c^\Gamma\}_{c=1}^{n^c}$, Eqs. (12) and (13) implicitly define tile edge lengths, say ℓ_1 and ℓ_2 , which should be equal to each other for the correct tile set setup. In our case, we sequentially check all values $\{n_c^\Gamma\}_{c=1}^{n^c}$ such that $n_c^\Gamma \geq 0$ and $\sum_{c=1}^{n^c} n_c^\Gamma \leq n^d$ and select the configuration with the minimum difference $|\ell_1 - \ell_2|$.⁵ On the basis of these data, we randomly generate positions of individual disks and assign them to randomly selected tiles, until an admissible configuration \mathbf{p} is obtained.

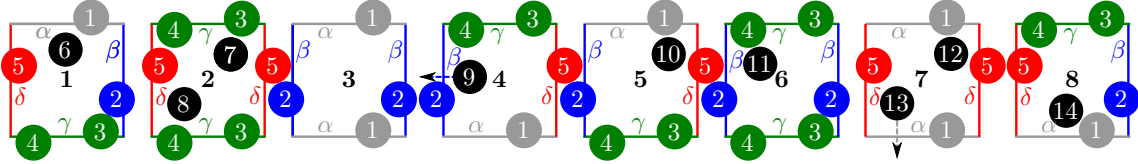


Figure 5: An example of an admissible $14\{1-1-2-1\}$ configuration (with $n_\alpha^\Gamma = n_\gamma^\Gamma = n_\delta^\Gamma = 1$ and $n_\beta^\Gamma = 2$ code-related disks) and its modification by disk displacements; disk 9 leaves its parent tile 4 and randomly enters tiles 1, 3, 6 or 8; disk 13 leaves its parent tile 7 and randomly enters tiles 1, 3, 5 or 7.

A single loop of the optimization algorithm involves a sequential selection of a disk $d = \{1, \dots, n^d\}$, and its movement given by

$$\hat{x}_j^{[d]} = x_j^{[d]} + \ell \left(U - \frac{1}{2} \right), \quad j = 1, 2, \quad (14)$$

repeated until a new admissible configuration $\hat{\mathbf{p}}$ is encountered. In Eq. (14), U denotes a random variable with a uniform distribution in the interval $[0, 1]$. If a disk, during its displacement, leaves its parent tile by crossing the edge with code c , it is randomly assigned to a tile sharing the same code, Fig. 5.

⁵Note that the values of ℓ and n^d are kept constant during the optimization process, whereas the values of n_c^Γ are allowed to change, since disks can move freely between tile interiors and edges.

The acceptance of a new solution $\hat{\mathbf{p}}$ is driven by the Metropolis criterion [20]

$$\exp\left(\frac{f(\mathbf{p}) - f(\hat{\mathbf{p}})}{T}\right) \geq U, \quad (15)$$

where T denotes the algorithmic temperature, initially set to T_{\max} and gradually reduced by a multiplicative constant $T_{\text{mlt}} < 1$ once the loop over all n^{d} disks is completed. The entire algorithm terminates after n_{\max} objective function evaluations. Moreover, we keep it restarting when the current temperature T is less than the threshold value T_{\min} .⁶ Such a step was found beneficial, as the resulting problem is highly multi-modal and discontinuous due to the presence of edge-constrained disks.

4. Results

The potential of the tile-based representation is demonstrated for the two-phase composite medium with the disk volume fraction $\phi = 26.8\%$, Fig. 3, with a moderate contrast in the material parameters⁷ and under the assumption of the plane strain state. Four distinct sets W8/2–2, differing in the tile edge length ℓ , the number of total and edge disks $n^{\text{d}}\{n^{\Gamma}\}_c^{n^c}$ used in the configuration and in the weight factor w balancing the geometrical and mechanical compatibility, have been examined, see Fig. 3. In particular, our aim to demonstrate that the proposed optimization algorithm works well for the tile morphology design and that the tile sets based on the specific tilings \mathcal{D}_S and \mathcal{D}_σ can be used to represent generic particulate media.

In Fig. 7, we present the disk configurations and two-point probability functions \tilde{S}_2 obtained for the domain \mathcal{D} being tiled by optimized tile sets. We observe that both reconstructed functions \tilde{S}_2 exhibit local peaks exceeding the value of ϕ^2 , which reveals the presence of characteristic length scales of order ℓ in the tiled medium. Nevertheless, the local extremes are notably smaller than the value of ϕ corresponding to a periodic construction, e.g. [26], and their number can be substantially reduced by increasing the edge length ℓ , Fig. 7(b).

Such conclusions are further supported by Fig. 8 showing cross-sections of the two-point probability functions in the k_1 direction for two different values of the weighting parameter w . The results demonstrate that for higher values of w , the

⁶All results reported below correspond to the following set of parameters: $T_{\max} = 10^{-3}$, $T_{\min} = 10^{-6}$, $T_{\text{mlt}} = (T_{\max}/T_{\min})^{1/200}$ and $n_{\max} = 10^4 n^{\text{d}}$.

⁷We set the Young modulus $E = 1$ and the Poisson ratio $\nu = 0.125$ for the matrix phase, while $E = 10$ and $\nu = 0.125$ for disks. All values are expressed in consistent units in what follows.

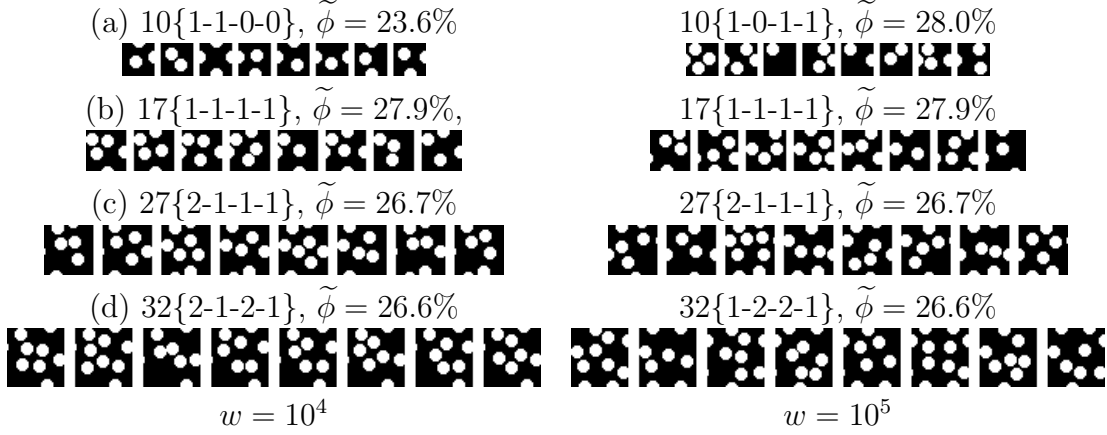


Figure 6: Optimized sets W8/2-2 obtained for weighting factors w equal to 10^4 and 10^5 and for configurations with (a) $n^d = 10$, $\ell = 42$ px, (b) $n^d = 17$, $\ell = 52$ px, (c) $n^d = 27$, $\ell = 64$ px and (d) $n^d = 38$, $\ell = 74$ px; $n^d\{n_c^\Gamma\}_{c=1}^{n_c}$ refers to configuration of n^d disks in total with n_c^Γ disks intersecting edge c , ℓ is the tile length and $\tilde{\phi}$ is the reconstructed volume fraction.

short-range phenomena are captured to a high accuracy and the magnitude of local extremes are consistently reduced with the increasing number of disks, albeit at a small rate. By decreasing the importance of S_2 -based reconstruction, Fig. 8(b), the discrepancy between the original and reconstructed medium substantially increases at short distances, leading even to inconsistent value of the volume fraction for 10 disks, and the local peaks become more pronounced as the stress-based criterion drives the system towards periodic media.

Fig. 9 illustrates the ability of the optimization algorithm to achieve self-compatible stress fields by comparing the distribution of the normal stresses σ_{11} obtained for an initial and the optimized configuration of disks. Clearly, the initial configuration exhibits significant stress jumps at contiguous edges, which are reduced to almost identical values by the proposed optimization algorithm.

To what extent are the stress fields obtained for the specific configuration \mathcal{D}_σ useful for a general tiling procedure? To address this question, we consider the reconstructed stress field $\tilde{\sigma}^{(i)}$, based on the fields found at eight tiles from top rows of the tiling, Fig. 10(d),⁸ assembled according to the template \mathcal{D}_σ . The local relative error associated with such replacement is quantified by

$$f_{\tilde{\sigma}}^{(i)}(\mathbf{k}) = \frac{\|\sigma^{(i)}(\mathbf{k}) - \tilde{\sigma}^{(i)}(\mathbf{k})\|_1}{\|\sigma^{(i)}(\mathbf{k})\|_1}, \quad \mathbf{k} \in \mathcal{K}^{\mathcal{D}_\sigma}, i = 1, 2, 3. \quad (16)$$

⁸It is worth noting that we have obtained analogous results for different selections of tiles 1–8.

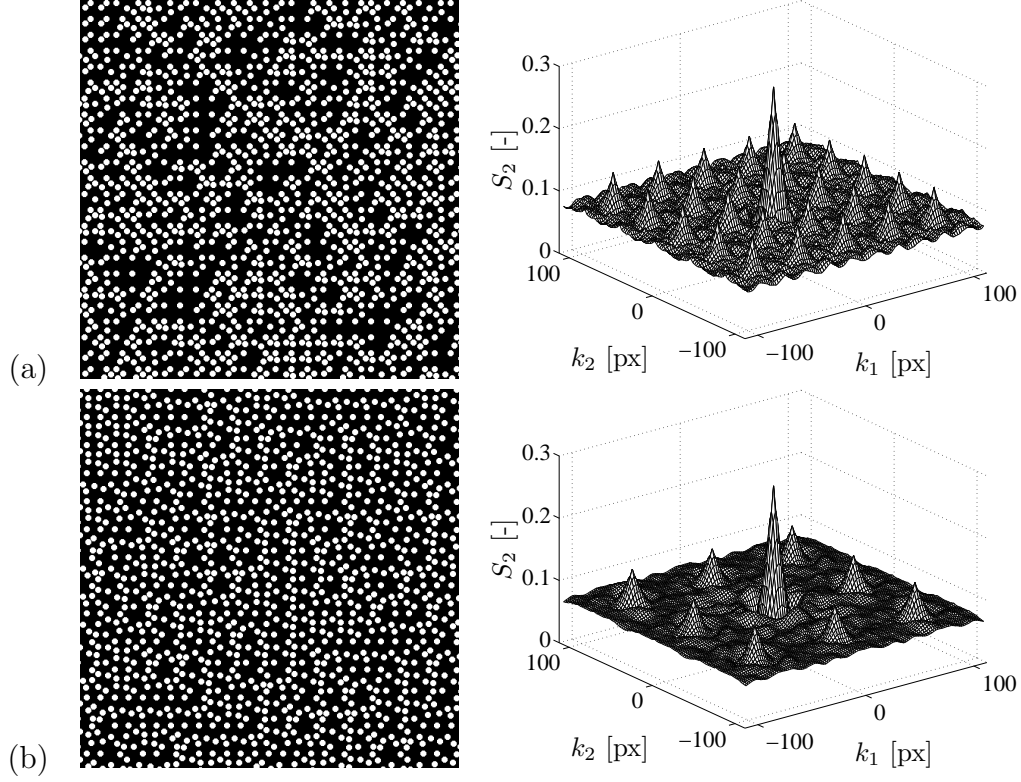


Figure 7: Reconstructed microstructures and two point probability functions \tilde{S}_2 for tile sets with (a) $n^d = 10$ disks and $\ell = 42$ px and (b) $n^d = 38$ disks and $\ell = 74$ px and identical weighting factors $w = 10^5$.

Outcomes of this comparison are shown in Fig. 10 in the form of tiling-based microstructures (a), distribution of the normal stress σ_{11} due to the loading by macroscopic shear strain (b), their reconstructed counterparts (c) and the spatial distribution of the relative error (d). For the microstructure generated from tiles with $n^d = 10$ disks, we observe that the reconstructed field displays significant distributed errors in tile interiors. Similarly to S_2 -based criterion, these deviations are significantly reduced and become highly localized when increasing the number of disks. This claim is further supported by Fig. 11, plotting the evolution of the average error

$$f_{\tilde{\sigma}} = \frac{1}{N^{\mathcal{D}_\sigma}} \sum_{i=1}^3 \sum_{\mathbf{k} \in \mathcal{K}^{\mathcal{D}_\sigma}} f_{\tilde{\sigma}}^{(i)}(\mathbf{k}) \quad (17)$$

as a function of the number of disks. For both values of w , we observe approximately

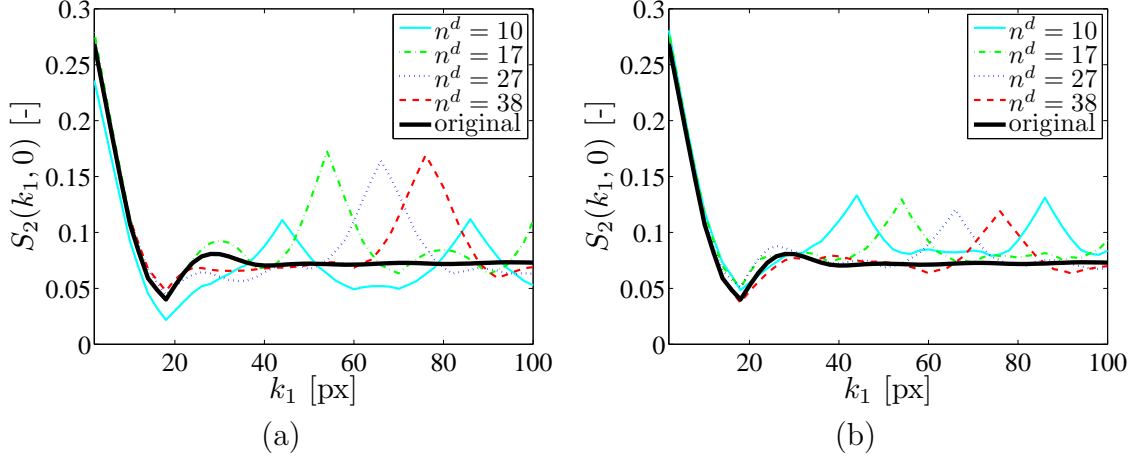


Figure 8: Comparison of two-point probability functions $S_2(k_1, 0)$ for the weighting factors (a) $w = 10^4$ and (b) $w = 10^5$.

linear convergence with respect to the number of disks n^d . Since the tile design has been based on different objective functions, this gives as yet another confirmation of their quality. Note that the significant compression has been achieved by the tiling-based representation: the original microstructure contains $\approx 1,300$ disks, whereas the most detailed tile-based representation builds only on 38 disks and is capable of producing much larger microstructures.

5. Enrichment strategies for finite element schemes

Consider a domain $\mathcal{O} \subset \mathbb{R}^2$ approximated by n^e finite elements Ω_e of characteristic size h , with the heterogeneity distribution quantified by a tiling $\tilde{\mathcal{O}} \supset \mathcal{O}$ based on an optimized tiled set, Fig. 12. The tiling also defines the “reconstructed” microstructure-induced perturbation displacement $\tilde{\mathbf{u}}^{*(i)} : \tilde{\mathcal{O}} \rightarrow \mathbb{R}^2$ or stress fields $\tilde{\boldsymbol{\sigma}}^{*(i)} : \tilde{\mathcal{O}} \rightarrow \mathbb{R}^3$, introduced in Eq. (A.6), associated with the i -th loadcase. The aim of this Section is to discuss two approaches of incorporating the reconstructed functions in the finite element schemes independently on the underlying element mesh.

The first strategy is based on the partition of unity method, introduced by Melenk and Babuška [5], and generalized in numerous aspects later on, e.g. [33, 34]. In this framework, we express the approximate solution in the form,

$$\mathbf{u}^h(\mathbf{x}) = \sum_{n=1}^{n^n} N_n(\mathbf{x}) \left[\mathbf{a}_n + \tilde{\mathbf{U}}^*(\mathbf{x}) \mathbf{b}_n \right] \text{ for } \mathbf{x} \in \mathcal{O}, \quad (18)$$

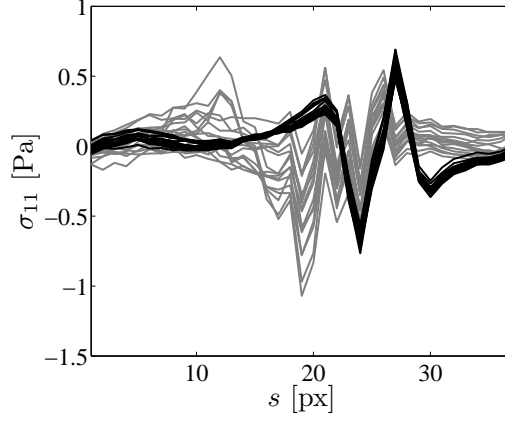


Figure 9: Distribution of the normal stress components σ_{11} due to loading by macroscopic strain $E_{12} = 1$ at edges Σ_δ of the tiling \mathcal{D}_σ , obtained for $n^d = 38$ disks with $w = 10^5$. The gray/black patterns correspond to initial/optimized morphologies, respectively.

where n^n is the number of nodes in the finite element mesh, $N_n : \mathcal{O} \rightarrow \mathbb{R}$ denotes the standard finite element basis functions, $\mathbf{a}_n \in \mathbb{R}^2$ and $\mathbf{b}_n \in \mathbb{R}^3$ stand for matrices of the standard and extended degrees of freedom associated with the n -th node. The matrix of enrichment functions $\tilde{\mathbf{U}}^* : \tilde{\mathcal{O}} \rightarrow \mathbb{R}^{2 \times 3}$ is defined as, cf. [13],

$$\tilde{\mathbf{U}}^*(\mathbf{x}) = \begin{bmatrix} \tilde{u}_1^{*(1)} & \tilde{u}_1^{*(2)} & \tilde{u}_1^{*(3)} \\ \tilde{u}_2^{*(1)} & \tilde{u}_2^{*(2)} & \tilde{u}_2^{*(3)} \end{bmatrix}(\mathbf{x}). \quad (19)$$

The ansatz (18) is then employed in the standard Galerkin procedure, following the exposition of Fish and Yuan [8, 9].

On the contrary, the Trefftz approach builds on the hybrid stress formulations developed by Teixeira de Freitas [6], see also [35] for an overview. It is based on the element stress approximation in the form

$$\boldsymbol{\sigma}^h(\mathbf{x}) = \mathbf{S}_e(\mathbf{x})\mathbf{a}_e + \tilde{\mathbf{S}}^*(\mathbf{x})\mathbf{b}_e \text{ for } \mathbf{x} \in \Omega_e, \quad (20)$$

where, analogously to Eq. (18), $\mathbf{S}_e \in \mathbb{R}^{3 \times m}$ stands for the standard basis functions of the Trefftz method associated with m regular degrees of freedom \mathbf{a}_e ; $\mathbf{b}_e \in \mathbb{R}^3$ denotes the extended degrees of freedom and the enrichment functions are obtained as

$$\tilde{\mathbf{S}}^*(\mathbf{x}) = \begin{bmatrix} \tilde{\sigma}_{11}^{*(1)} & \tilde{\sigma}_{11}^{*(2)} & \tilde{\sigma}_{11}^{*(3)} \\ \tilde{\sigma}_{22}^{*(1)} & \tilde{\sigma}_{22}^{*(2)} & \tilde{\sigma}_{22}^{*(3)} \\ \tilde{\sigma}_{12}^{*(1)} & \tilde{\sigma}_{12}^{*(2)} & \tilde{\sigma}_{12}^{*(3)} \end{bmatrix}(\mathbf{x}). \quad (21)$$

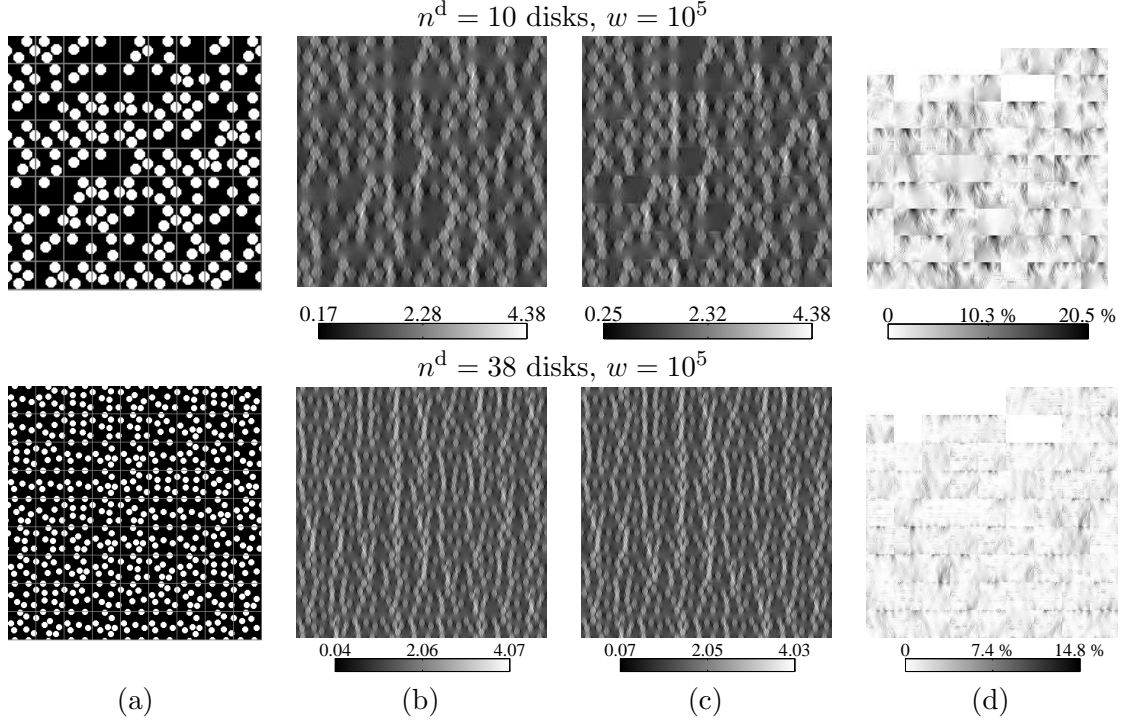


Figure 10: Assessment of tiling-based distribution of local fields, (a) microstructure obtained by tile \mathcal{D}_σ , distribution of (b) local stress fields $\sigma_{11}^{(3)}$, (c) reconstructed stress fields $\tilde{\sigma}_{11}^{(3)}$ and of the (d) reconstruction-based error $f_\sigma^{(3)}$.

Note that the regular and enriched basis functions are selected such that the stress $\boldsymbol{\sigma}^h$ remains self-equilibrated. This is complemented with an independent approximation of displacements at the element boundary Γ_e

$$\mathbf{u}^h(\mathbf{x}) = \mathbf{N}_e^\Gamma(\mathbf{x})\mathbf{a}_e^\Gamma \text{ for } \mathbf{x} \in \Gamma_e, \quad (22)$$

involving only regular (macroscopic) shape functions and standard set of degrees of freedom. The remainder of the formulation follows from the weak form of the equilibrium and compatibility equations, which can be converted to the element boundaries by virtue of the divergence theorem, cf. [6, 36]. Note that the particular scheme developed in [13] eliminates the extended degrees of freedom \mathbf{b}_e by coupling them to the average strain in the matrix phase with the stiffness matrix \mathbf{L}^m in the following fashion:

$$\mathbf{b}_e = \frac{1}{|\Omega_e|} (\mathbf{L}^m)^{-1} \left(\int_{\Omega_e} \mathbf{S}_e(\mathbf{x}) d\mathbf{x} \right) \mathbf{a}_e. \quad (23)$$

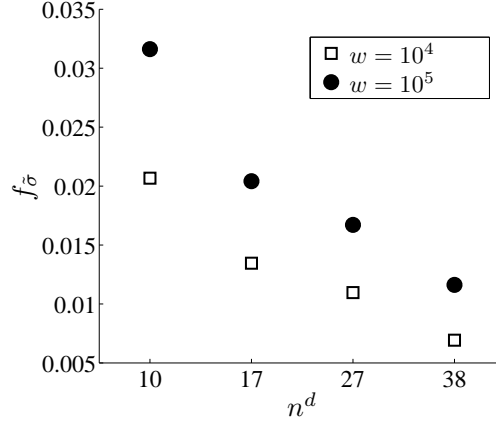


Figure 11: Relative stress error $f_{\tilde{\sigma}}$ as a function of the number of disks for different weights w .

This step has been found to substantially increase the computational efficiency, while maintaining a high accuracy of the resulting fields.

6. Conclusions

In this work, we have proposed a novel approach to the construction of aperiodic local fields in heterogeneous media with potential applications in hybrid FE environments. The method is based on the Wang tiling concept that allows us to represent complex patterns using a limited set of basic tiles, complemented by the Simulated Annealing-based algorithm to arrive at the optimal tile set morphology. On the basis on the results obtained for stress analyses in two-dimensional particulate media we conjecture that:

- the proposed method provides a robust tool for compression of disordered microstructures and can serve as an efficient microstructure generation algorithm,
- it allows for aperiodic extensions of local, possibly periodic, fields to substantially larger domains while maintaining their compatibility,
- the tiling-based fields can be used to produce microstructure-based enrichment functions for generalized Partition of Unity methods or hybrid finite element schemes.

We are fully aware that our conclusions are somewhat provisional, in the sense that these are based on a single set of tiles and the specific class of microstructures. Extending the current results to general setting is in the focus of our current work.

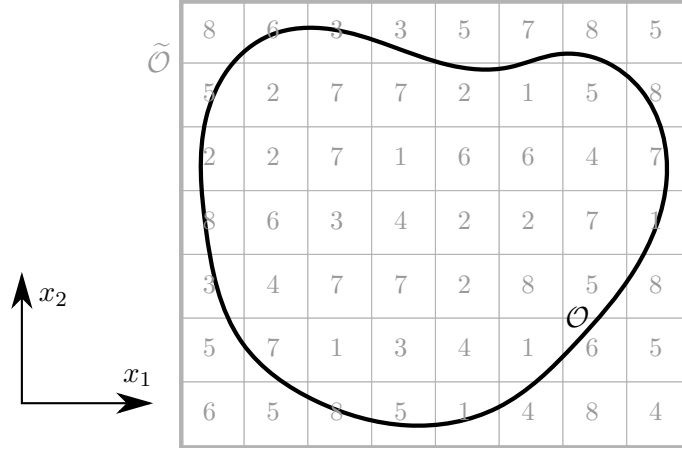


Figure 12: Domain \mathcal{O} with heterogeneity distribution described by tiling $\tilde{\mathcal{O}}$.

Acknowledgments. The authors thank Jaroslav Vondřejc (CTU in Prague) for providing us with a MATLAB source code of FFT-based homogenization algorithm and Adrian Russell (University of New South Wales) and Michal Šejnoha (CTU in Prague) for helpful comments on the manuscript. We also gratefully acknowledge financial support by Australian Research Council (grants: LP0990054, LP100100806), Czech Science Foundation (grants: 103/09/P490, 105/11/0411) and The Ministry of Education, Youth and Sports of the Czech Republic (grant: MSM6840770003).

Appendix A. Computation of mechanical fields

As explained earlier in Section 3.2, our objective is to determine local fields within the tiling $\mathcal{D}_\sigma \subset \mathbb{R}^2$ subjected to a given macroscopic strain field $\mathbf{E} \in \mathbb{R}^{2 \times 2}$ under the periodic boundary conditions. These follow from the solution of the elastic unit cell problem [22, 37]

$$\boldsymbol{\varepsilon}(\mathbf{x}) = \frac{1}{2} (\nabla \mathbf{u}(\mathbf{x}) + \nabla \mathbf{u}(\mathbf{x})^\top), \quad \nabla \cdot \boldsymbol{\sigma}(\mathbf{x}) = \mathbf{0}, \quad \boldsymbol{\sigma}(\mathbf{x}) = \mathbf{L}(\mathbf{x}) \boldsymbol{\varepsilon}(\mathbf{x}), \quad (\text{A.1})$$

in which $\boldsymbol{\sigma} : \mathcal{D}_\sigma \rightarrow \mathbb{R}^{2 \times 2}$ denotes the symmetric \mathcal{D}_σ -periodic second-order stress tensor field, $\mathbf{u} : \mathcal{D}_\sigma \rightarrow \mathbb{R}^2$ designates the displacement field, $\mathbf{L} : \mathcal{D}_\sigma \rightarrow \mathbb{R}^{2 \times 2 \times 2 \times 2}$ is the symmetric positive-definite fourth-order tensor of materials stiffness and $\boldsymbol{\varepsilon} : \mathcal{D}_\sigma \rightarrow \mathbb{R}^{2 \times 2}$ is the \mathcal{D}_σ -periodic strain field satisfying

$$\frac{1}{|\mathcal{D}_\sigma|} \int_{\mathcal{D}_\sigma} \boldsymbol{\varepsilon}(\mathbf{x}) \, d\mathbf{x} = \mathbf{E}. \quad (\text{A.2})$$

It is well-known [37, 22] that the solution to the unit cell is characterized by the Lippman-Schwinger equation

$$\boldsymbol{\varepsilon}(\mathbf{x}) + \int_{\mathcal{D}_\sigma} \boldsymbol{\Gamma}(\mathbf{x} - \mathbf{y}) \delta \mathbf{L}(\mathbf{y}) \boldsymbol{\varepsilon}(\mathbf{y}) \, \mathrm{d}\mathbf{y} = \mathbf{E}, \quad (\text{A.3})$$

where $\delta \mathbf{L} = \mathbf{L} - \mathbf{L}_0$, $\mathbf{L}_0 \in \mathbb{R}^{2 \times 2 \times 2 \times 2}$ is an auxiliary positive definite stiffness tensor of a reference medium and the fourth-order tensor $\boldsymbol{\Gamma} : \mathcal{D}_\sigma \rightarrow \mathbb{R}^{2 \times 2 \times 2 \times 2}$ is related to the Green function of the problem (A.1) with $\mathbf{L}(\mathbf{x}) = \mathbf{L}_0$. It admits a compact closed-form expression in the Fourier space, e.g. [37, Section 5.3], and its action can be efficiently evaluated by the FFT algorithm. This observation is at the heart of an iterative scheme due to Moulinec and Suquet [38], which can be applied to arbitrary digitized media.

In our case, we adopt an accelerated version of the original algorithm based on observations due to Zeman *et al.* [39]. Since the sample is discretized by a regular $N_1^{\mathcal{D}_\sigma} \times N_2^{\mathcal{D}_\sigma}$ bitmap, it is convenient to project the integral equation onto the space of trigonometric polynomials, e.g. [40]. This yields the linear system in the form

$$(\mathbf{I} + \mathbf{B})\mathbf{e} = \mathbf{E}, \quad (\text{A.4})$$

where $\mathbf{e} \in \mathbb{R}^{3 \times N_1^{\mathcal{D}_\sigma} \times N_2^{\mathcal{D}_\sigma}}$ stores the unknown stress values at individual pixels, $\mathbf{E} \in \mathbb{R}^{3 \times N_1^{\mathcal{D}_\sigma} \times N_2^{\mathcal{D}_\sigma}}$ is the corresponding matrix of overall strains and matrix \mathbf{B} is expressed as a product of several matrices

$$\begin{aligned} \mathbf{B} &= \begin{pmatrix} \mathbf{F}^{-1} & \mathbf{0} & \mathbf{0} \\ \mathbf{0} & \mathbf{F}^{-1} & \mathbf{0} \\ \mathbf{0} & \mathbf{0} & \mathbf{F}^{-1} \end{pmatrix} \begin{pmatrix} \boldsymbol{\Gamma}_{1111} & \boldsymbol{\Gamma}_{1122} & \sqrt{2}\boldsymbol{\Gamma}_{1112} \\ \boldsymbol{\Gamma}_{2211} & \boldsymbol{\Gamma}_{2222} & \sqrt{2}\boldsymbol{\Gamma}_{1112} \\ \sqrt{2}\boldsymbol{\Gamma}_{2212} & \sqrt{2}\boldsymbol{\Gamma}_{1212} & 2\boldsymbol{\Gamma}_{2212} \end{pmatrix} \begin{pmatrix} \mathbf{F} & \mathbf{0} & \mathbf{0} \\ \mathbf{0} & \mathbf{F} & \mathbf{0} \\ \mathbf{0} & \mathbf{0} & \mathbf{F} \end{pmatrix} \\ &\times \begin{pmatrix} \delta \mathbf{L}_{1111} & \delta \mathbf{L}_{1122} & \sqrt{2}\delta \mathbf{L}_{1112} \\ \delta \mathbf{L}_{2211} & \delta \mathbf{L}_{2222} & \sqrt{2}\delta \mathbf{L}_{1112} \\ \sqrt{2}\delta \mathbf{L}_{2212} & \sqrt{2}\delta \mathbf{L}_{1222} & 2\delta \mathbf{L}_{2212} \end{pmatrix}. \end{aligned} \quad (\text{A.5})$$

Here, $\mathbf{F} \in \mathbb{C}^{N_1^{\mathcal{D}_\sigma} \times N_2^{\mathcal{D}_\sigma}}$ and \mathbf{F}^{-1} implement the forward and the inverse Fourier transform and, e.g., $\delta \mathbf{L}_{1122} \in \mathbb{R}^{N_1^{\mathcal{D}_\sigma} \times N_2^{\mathcal{D}_\sigma}}$ stores the corresponding component of the stiffness tensor at individual pixels, see [39] for more details. The system (A.4) is solved using standard conjugate gradient algorithm. Upon convergence, the distribution of the local stress field $\boldsymbol{\sigma}$ is determined from the solution \mathbf{e} by Eq. (A.1)₃. Note that the construction of the enrichment functions in Section 5 is based on the perturbation fields of displacements and stresses

$$\mathbf{u}^*(\mathbf{x}) = \mathbf{u}(\mathbf{x}) - \frac{1}{|\mathcal{D}_\sigma|} \int_{\mathcal{D}_\sigma} \mathbf{u}(\mathbf{y}) \, \mathrm{d}\mathbf{y}, \quad \boldsymbol{\sigma}^*(\mathbf{x}) = \boldsymbol{\sigma}(\mathbf{x}) - \frac{1}{|\mathcal{D}_\sigma|} \int_{\mathcal{D}_\sigma} \boldsymbol{\sigma}(\mathbf{y}) \, \mathrm{d}\mathbf{y}, \quad (\text{A.6})$$

instead of the total values. Both quantities can be efficiently obtained from the known strain and stress fields in the Fourier space, e.g., [41].

References

- [1] J. Oden, T. Belytschko, J. Fish, T. Hughes, C. Johnson, D. Keyes, A. Laub, L. Petzold, D. Srolovitz, S. Yip, Simulation-based engineering science: Revolutionizing engineering science through simulation, Report of the National Science Foundation blue ribbon panel on simulation-based engineering science, National Science Foundation, Arlington, VA, available at http://www.nsf.gov/pubs/reports/sbes_final_report.pdf (2006).
- [2] F. Feyel, J.-L. Chaboche, FE^2 multiscale approach for modelling the elastoviscoplastic behaviour of long fibre SiC/Ti composite materials, *Computer Methods in Applied Mechanics and Engineering* 183 (3-4) (2000) 309–330.
- [3] B. Pichler, S. Scheiner, C. Hellmich, From micron-sized needle-shaped hydrates to meter-sized shotcrete tunnel shells: Micromechanical upscaling of stiffness and strength of hydrating shotcrete, *Acta Geotechnica* 3 (4) (2008) 273–294.
- [4] M. Geers, V. Kouznetsova, W. Brekelmans, Multi-scale computational homogenization: Trends and challenges, *Journal of Computational and Applied Mathematics* 234 (2010) 2175–2182.
- [5] J. M. Melenk, I. Babuška, The partition of unity finite element method: Basic theory and applications, *Computer Methods in Applied Mechanics and Engineering* 139 (1-4) (1996) 289 – 314.
- [6] J. Teixeira de Freitas, Formulation of elastostatic hybrid-Trefftz stress elements, *Computer Methods in Applied Mechanics and Engineering* 153 (1998) 127–151.
- [7] A. Matache, I. Babuška, C. Schwab, Generalized p -FEM in homogenization, *Numerische Mathematik* 86 (2000) 319–375.
- [8] J. Fish, Z. Yuan, Multiscale enrichment based on partition of unity, *International Journal for Numerical Methods in Engineering* 62 (10) (2005) 1341–1359.
- [9] J. Fish, Z. Yuan, Multiscale enrichment based on partition of unity for nonperiodic fields and nonlinear problems, *Computational Mechanics* 40 (2007) 249–259.

- [10] F. K. F. Radtke, A. Simone, L. J. Sluys, A partition of unity finite element method for obtaining elastic properties of continua with embedded thin fibres, *International Journal for Numerical Methods in Engineering* 84 (6) (2010) 708–732.
- [11] F. K. F. Radtke, A. Simone, L. J. Sluys, A partition of unity finite element method for simulating non-linear debonding and matrix failure in thin fibre composites, *International Journal for Numerical Methods in Engineering* 86 (4–5) (2011) 453–476.
- [12] I. Babuška, R. Lipton, Optimal local approximation spaces for generalized finite element methods with application to multiscale problems, *Multiscale Modeling and Simulation* 9 (1) (2011) 373–406. [arXiv:1004.3041](#).
- [13] J. Novák, L. Kaczmarczyk, P. Grassl, J. Zeman, C. Pearce, A micromechanics-enhanced a finite element formulation for modelling heterogeneous materials, *Computer Methods in Applied Mechanics and Engineering*, Accepted manuscript. [arXiv:1103.5633](#), [doi:10.1016/j.cma.2011.09.003](#).
- [14] H. Wang, Proving theorems by pattern recognition–II, *Bell Systems Technical Journal* 40 (2) (1961) 1–41.
- [15] A. Glassner, Andrew Glassner’s notebook, *Computer Graphics and Applications*, *IEEE* 24 (1) (2004) 86–91.
- [16] K. Culik, An aperiodic set of 13 Wang tiles, *Discrete Mathematics* 160 (1996) 245–251.
- [17] M. Cohen, J. Shade, S. Hiller, O. Deussen, Wang tiles for image and texture generation, *ACM Transactions on Graphics* 22 (3) (2003) 287–294.
- [18] E. Demaine, M. Demaine, Jigsaw puzzles, edge matching, and polyomino packing: Connections and complexity, *Graphs and Combinatorics* 23 (2007) 195–208.
- [19] A. Lagae, P. Dutré, A comparison of methods for generating Poisson disk distributions, *Computer Graphics Forum* 27 (1) (2008) 114–129.
- [20] S. Kirkpatrick, C. J. Gelatt, M. P. Vecchi, Optimization by simulated annealing, *Science* 220 (1983) 671–680.
- [21] J. Černý, Thermodynamical approach to the traveling salesman problem: An efficient simulation algorithm, *Journal of Optimization Theory and Applications* 45 (1985) 41–51.

- [22] G. W. Milton, The Theory of Composites, Vol. 6 of Cambridge Monographs on Applied and Computational Mathematics, Cambridge University Press, 2002.
- [23] G. L. Povirk, Incorporation of microstructural information into models of two-phase materials, *Acta Metallurgica et Materialia* 43 (8) (1995) 3199–3206.
- [24] C. L. Y. Yeong, S. Torquato, Reconstructing random media, *Physical Review E* 57 (1) (1998) 495–506.
- [25] H. Kumar, C. Briant, W. Curtin, Using microstructure reconstruction to model mechanical behavior in complex microstructures, *Mechanics of Materials* 38 (8–10) (2006) 818–832.
- [26] J. Zeman, M. Šejnoha, From random microstructures to representative volume elements, *Modelling and Simulation in Materials Science and Engineering* 15 (4) (2007) S325–S335, 2007 Highlight paper.
- [27] H. Lee, M. Brandyberry, A. Tudor, K. Matouš, Three-dimensional reconstruction of statistically optimal unit cells of polydisperse particulate composites from microtomography, *Physical Review E* 80 (2009) 061301.
- [28] S. Niezgoda, D. Turner, D. Fullwood, S. Kalidindi, Optimized structure based representative volume element sets reflecting the ensemble-averaged 2-point statistics, *Acta Materialia* 58 (13) (2010) 4432–4445.
- [29] J. Schröder, D. Balzani, D. Brands, Approximation of random microstructures by periodic statistically similar representative volume elements based on lineal-path functions, *Archive of Applied Mechanics* 81 (2011) 975–997.
- [30] S. Torquato, Random heterogenous materials, Springer-Verlag, New York, 2002.
- [31] J. Gajdošík, J. Zeman, M. Šejnoha, Qualitative analysis of fiber composite microstructure: Influence of boundary conditions, *Probabilistic Engineering Mechanics* 21 (4) (2006) 317–329.
- [32] M. Lepš, Single and multi-objective optimization in civil engineering with applications, Ph.D. thesis, CTU in Prague, available at <http://klobouk.fsv.cvut.cz/~leps/publications/pdf/thesis.pdf> (2005).
- [33] T. Belytschko, R. Gracie, G. Ventura, A review of extended/generalized finite element methods for material modeling, *Modelling and Simulation in Materials Science and Engineering* 17 (4) (2009) 043001.

- [34] T.-P. Fries, T. Belytschko, The extended/generalized finite element method: An overview of the method and its applications, *International Journal for Numerical Methods in Engineering* 84 (3) (2010) 253–304.
- [35] I. Herrera, Trefftz method: a general theory, *Numerical Methods for Partial Differential Equations* 16 (6) (2000) 561–580.
- [36] Ł. Kaczmarczyk, C. J. Pearce, A corotational hybrid-Trefftz stress formulation for modelling cohesive cracks, *Computer Methods in Applied Mechanics and Engineering* 198 (15–16) (2009) 1298–1310.
- [37] J. Michel, H. Moulinec, P. Suquet, Effective properties of composite materials with periodic microstructure: a computational approach, *Computer Methods in Applied Mechanics and Engineering* 172 (1-4) (1999) 109 – 143.
- [38] H. Moulinec, P. Suquet, A fast numerical method for computing the linear and nonlinear mechanical properties of composites, *Comptes rendus de l’Académie des sciences. Série II, Mécanique, physique, chimie, astronomie* 318 (11) (1994) 1417–1423.
- [39] J. Zeman, J. Vondřejc, J. Novák, I. Marek, Accelerating a FFT-based solver for numerical homogenization of periodic media by conjugate gradients, *Journal of Computational Physics* 229 (21) (2010) 8065–8071. [arXiv:1004.1122](#).
- [40] J. Saranen, G. Vainikko, *Periodic Integral and Pseudodifferential Equations with Numerical Approximation*, Springer Monographs in Mathematics, Springer-Verlag, Berlin, Heidelberg, 2002.
- [41] F. Willot, Y.-P. Pellegrini, M. I. Idiart, P. P. Castañeda, Effective-medium theory for infinite-contrast two-dimensionally periodic linear composites with strongly anisotropic matrix behavior: Dilute limit and crossover behavior, *Physical Review B* 78 (2008) 104111. [arXiv:0804.2817](#).